

# Open or Closed? Elucidating the Correlation between Micropore Nature and Sodium Storage Mechanisms in Hard Carbon

Vishnu Surendran,<sup>[a]</sup> Radhika Krishna Hema,<sup>[a]</sup> Muhammed Shafeek Olyantakath Hassan,<sup>[b]</sup> Vinesh Vijayan,<sup>[b]</sup> and Manikoth M. Shajumon<sup>\*[a]</sup>

The sodium storage mechanism related to a high voltage slope region and a low voltage plateau region observed commonly in hard carbon (HC) is still a topic of debate. The difference in physicochemical properties of controllably synthesized carbon reflects the ambiguity in explaining their charge storage mechanism. Herein, we attempt to unravel the sodium storage mechanism using HCs with controlled 'closed' and 'open' porosities. Opening the 'closed' pores diminishes the plateau

region but does not affect the slope region. Electrochemical measurements coupled with N<sub>2</sub> and CO<sub>2</sub> gas adsorption studies reveal a strong correlation between closed pores with a diameter ( $d$ ),  $0.4 < d < 1.5$  nm and capacity contribution from the plateau region, supporting the adsorption/intercalation-pore filling model. Solid-state NMR measurements confirm the near metallic state of sodium in the 'closed' micropores of HCs at potentials close to 0 V (vs. Na).

## Introduction

Hard carbons (HC) are well-considered and investigated as sodium-ion battery (SIB) anodes due to their economic feasibility, environmental friendliness, and easily available bioresources. In light of research, they offer high specific capacity, cycling stability, sufficiently low operating voltages, and possess expanded interlayers ( $d$  ranging from 3.7 to 4 Å).<sup>[1–5]</sup> The widely accepted structure of HCs has been the 'house of cards' model suggested by Dahn and Stevens in 2000, wherein they propound that the turbostratic/pseudo graphitic domains are randomly distributed (randomness at a relatively large scale) with graphene sheets, inducing short-range ordering unlike that in graphite.<sup>[6]</sup> For the same objective, the precursor is expected to have a highly branched and crosslinked matrix that can avert long-range ordered graphitization even at high carbonization temperatures. It is well known that the microstructure and morphology of HCs remain intact even after heat treatment, contrary to soft carbons (graphitizable carbon), which enter a fluid phase thereafter.<sup>[7]</sup> Above all, the atomic arrangement after carbonization shall be different for different precursors, each attaining a stable configuration in terms of energy as validated by Yamamoto *et al.*<sup>[8]</sup> This is realized *via* migration of carbon atoms, formation of new bonds or creation of vacancies by hydrogen, and any

heteroatom release or even reorientation, creating porosity.<sup>[2]</sup> Such "storage sites" in HCs lead the way to manifold possibilities of incorporating sodium ions via pore-filling, intercalation between graphene sheets, surface adsorption, and defect-binding.<sup>[1,9–12]</sup>

A proper notion of how exactly are HCs facilitating sodiation/desodiation would help in realizing their implementation, thereby advocating sustainable energy management. Several mechanistic models have been proposed, and it is unarguable that the sodium storage behavior cannot be considered in abstraction to the structural variations in HCs. Commonly, two distinct voltage regions are observed in the galvanostatic charge/discharge profiles of HCs: a sloping curve above 0.1 V vs. Na/Na<sup>+</sup> and a flat plateau below 0.1 V vs. Na/Na<sup>+</sup>. Discussions were initiated when Dahn and Stevens documented a two-step mechanism using the "insertion-filling" model in their work on glucose-pyrolyzed HCs.<sup>[13]</sup> Besides many groups reaffirming the model,<sup>[14]</sup> Stratford *et al.* were later able to demonstrate a shift of Na NMR peak from that of Na(I) towards Na(0) in the plateau region, in agreement with the pore filling at low potentials.<sup>[15]</sup> Over the years, the sloping nature was attributed to reversible adsorption onto edges, functional groups, and defects, including heteroatoms, alongside the perception that the process occurs at sites with energy distributed within a range. Before long, there was an upsurge in studies suggesting that intercalation could be the origin of the plateau in the voltage profile, thereby endorsing the "adsorption-insertion" model.<sup>[16]</sup> Confuting the existing schemes, Tarascon and co-workers manifested an "adsorption-filling" mechanism with almost similar characterization tools as already employed.<sup>[17]</sup> The suggestion was reemphasized by Bai *et al.* in a rather interesting way by infusing sulfur into the HC micropores which resulted in the disappearance of the plateau.<sup>[9]</sup> A model named "extended adsorption-insertion" was later postulated wherein carbon domains were classified

[a] Dr. V. Surendran, R. K. Hema, Prof. M. M. Shajumon

School of Physics

Indian Institute of Science Education and Research Thiruvananthapuram  
Maruthamala PO, Vithura, Thiruvananthapuram, Kerala 695551, India  
E-mail: shajju@iisertvm.ac.in

[b] M. S. O. Hassan, Prof. V. Vijayan

School of Chemistry

Indian Institute of Science Education and Research Thiruvananthapuram  
Maruthamala PO, Vithura, Thiruvananthapuram, Kerala 695551, India

 Supporting information for this article is available on the WWW under  
<https://doi.org/10.1002/batt.202200316>

according to the interlayer spacing with the corresponding mechanism sorted.<sup>[18]</sup> Notably, the study utilized the profile-fitting method for (002) peak in XRD studies to demonstrate that the evolution of carbon phases with the temperature appears rather gradual with the co-existence of individual domains, making it strenuous to settle upon a single mechanism. What is more, it later transpired that the porosity analysis of HCs would require the internal/closed porosity to be particularly attended to. Reports have suggested the plausibility of open and closed porosity contributing differently to the sodium storage in HCs at low potentials.<sup>[19–21]</sup> The commonly adopted nitrogen adsorption studies could disregard and overlook the contribution from closed pores, and hence it entails putting small-angle X-ray scattering (SAXS) into further use.<sup>[2]</sup> SAXS aids the inclusion of both closed (bulk) and open (surface) porosity in the measurements but is limited to proposing an average pore size. Researchers have as well employed HRTEM to confirm the presence of closed pores and true density measurements to quantify the same.<sup>[19,20]</sup>

Despite constant efforts by researchers to understand the structure-mechanism correlation of sodium storage in HCs, a universal model is impending to be concluded. It can be discerned that most of the studies did focus on tuning the microstructure in the desire to mitigate constraints. Contradicting interpretations drawn by different research teams might be a consequence of the distinctive characterization tools and precursors used, in addition to the failure to clearly unravel the host's structure, each of them with microstructure and porosity differing greatly from another's. Therefore, the controlled synthesis of samples is the key to shedding light on mechanistic insights. Unfortunately, the most common method adopted by the researchers to develop controlled samples is carbonizing the precursor at different temperatures with or without adding additional chemicals. Commonly observed phenomena upon high-temperature pyrolysis are, decreased  $d$  spacing and increased crystal size of graphitic domains, decreased curvature, micropore contribution and plateau capacity.<sup>[22–26]</sup> Simultaneous change in multiple physical properties create extreme difficulty in associating discharge nature with the nature of carbon material.

Taking all these aspects into consideration, herein, we attempt to unravel the sodium storage mechanism *via* a controlled porosity approach using HCs derived from coconut sprouts. Coconut sprouts are bulk, spongy masses formed from coconut seeds during germination, serving the purpose of nourishing the embryo. Studies show that sprouts are composed of highly degraded ligno-cellulosic matrices embedded with simple sugars, essentially glucose and fructose.<sup>[27]</sup> The branched, non-crystalline, and crosslinked matrices rich in lignin would ensure dismissal of any large-scale graphitic ordering even at high pyrolysis temperatures,<sup>[28]</sup> and hence coconut sprout was chosen as the material of interest. Scads of previous studies focused on differing the pyrolysis temperature to vary the porosities. However, low-temperature treatments ensure sufficient porosity while not being detrimental to the intact framework of the precursor, unlike activations performed at high temperatures.<sup>[28,29]</sup> That said, we have considered low-

temperature air-activation after carbonization to introduce additional porosity. We could observe a not gradual but abrupt disappearance of the flat plateau upon air activation, which urged us to elaborate more on the contributions of bulk porosity at low potentials. Our findings, well supported by controlled porosity and solid-state NMR measurements, suggest the occurrence of kinetically faster pseudocapacitive adsorption onto defects/insertion into graphitic layers at high potentials whilst the plateau at low potentials is actuated by the closed pores in the HC.

## Results and Discussion

Different carbon materials were synthesized by varying carbonization and air activation temperature along with the duration of activation, with the aim of tuning micro porosity without changing the bulk crystallinity. Three carbon materials that showed a trend in physical and electrochemical properties were picked out of the five samples (Table S1). The materials under the point of interest are CSDHC, CSDHC 280/15 and CSDHC 300/30. This series of materials are initially carbonized at 1000 °C and later air-activated at low temperatures. SEM images of CSDHC, CSDHC 280/15 and CSDHC 300/30 indicate all carbons samples have a similar structure with particle size around 8–10 μm (Figure 1A–C). CSDHC 280/15 and CSDHC 300/30 retained their structure even after the temperature treatments in the oxygen atmosphere. High-resolution transmission electron microscopy (HRTEM) images of non-activated and activated samples (Figure 1D–I) are very similar, indicating that air activation does not alter the microcrystalline nature of CSDHC.

Curly pseudo graphitic fringes are visible in all matrices, and scattered carbon fragments without exhibiting any long-range order are observable in the samples. The results are in accordance with the claim that the crosslinking in sprout aid short-range order. The average interlayer distance ( $d$  spacing) of CSDHC, CSDHC 280/15 and CSDHC 300/30 is found to be 0.394 nm, 0.398 nm, and 0.391 nm, respectively, using image processing software (Image J). Assessment of nitrogen adsorption isotherms provides additional insights into the micro-porosity of materials over TEM. N<sub>2</sub> adsorption isotherm (Figure 2A) of CSDHC and CSDHC 280/15 are of Type II with H3 hysteresis resulting from incompletely filled pore condensate in the macropores.<sup>[30]</sup> In contrast, N<sub>2</sub> adsorption isotherm of CSDHC 300/30 revealed that it is of type H4 hysteresis, with the pore size distribution implying the matrices air-activated at 300 °C are generously microporous (pore diameter ~0.55 nm) (Figure 2B). There is a significant increment in the microporosity (contribution of pores with a diameter lesser than 2 nm) and the BET surface area from 40 m<sup>2</sup> g<sup>-1</sup> to 655 m<sup>2</sup> g<sup>-1</sup> on activation for 30 minutes at 300 °C. Pore volume calculated for CSDHC is 0.068 cm<sup>3</sup> g<sup>-1</sup>, and that for CSDHC 300/30 is 0.424 cm<sup>3</sup> g<sup>-1</sup>, which is nearly six times more than the CSDHC. Dahn and co-workers have made similar observations in their earlier studies of lithium storage in hard carbons,<sup>[31]</sup> and observed that even a small burn-off of less than 5% can shoot the BET area of the

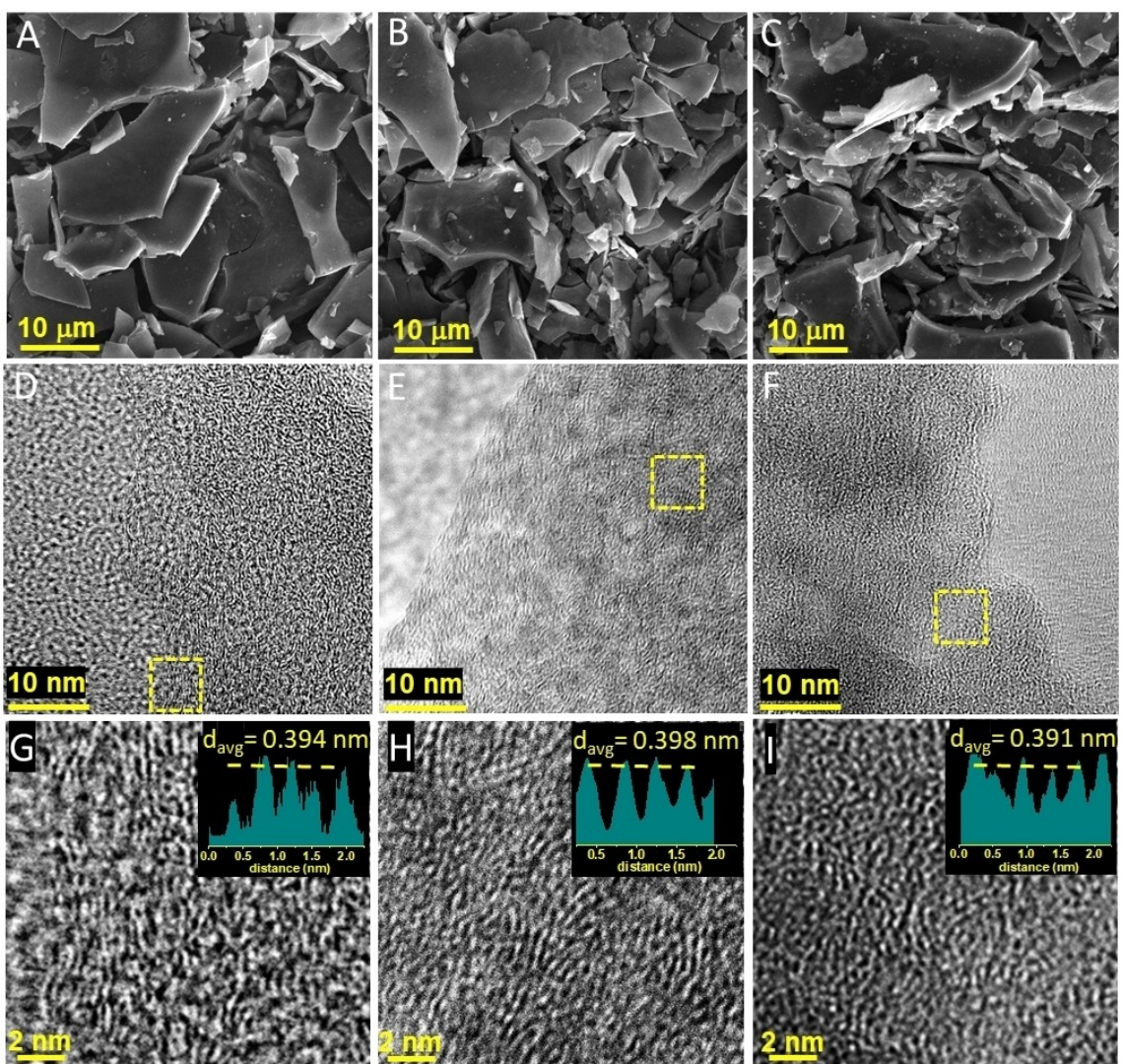


**Figure 1.** SEM images of A) 1000 °C annealed (CSDHC), B) air activated at 280 °C for 15 min (CSDHC 280/15), C) air activated at 300 °C for 30 min (CSDHC 300/30), which reveal air activation did not alter their macroscopic structure. TEM images of D) 1000 °C annealed, E) air activated at 280 °C for 15 min and F) air activated at 300 °C for 30 min samples. G–I) are the zoomed images of the area marked in yellow rectangles in (D–F), respectively. Inset of (G–I) are the plot profile of the curly domains drawn using ImageJ software. Average  $d$  spacing and curly appearance of matrices are similar in all three samples, indicating the microcrystalline structures are not affected by air activation.

carbon sample. This could be highly correlated with the nature of carbon precursors used. Thermogravimetric analysis (TGA) curves obtained for the sample CSDHC heated under oxygen flow at a ramp rate of 5 °C exhibited a weight loss not until 280 °C (Figure S1). A 3.55 % weight loss was recorded when the system was held at 300 °C for 1 h. TGA analysis indicates air annealing causes carbon burn-off, transforming the material to microporous nature. Even the shortest exposure time of 3 minutes made the CSDHC highly porous (Table S1).

Due to the slow diffusion kinetics, ultra-micropores ( $\sim < 0.7$  nm) are inaccessible to nitrogen molecules at 77 K; hence, we employed carbon dioxide adsorption measurements at 273 K to probe the “closed” pores.<sup>[32]</sup> We define the “closed pores” as the nitrogen inaccessible vacant spaces. Interestingly, the carbon dioxide adsorption isotherm (Figure 2C) reveals that the gas intake of all samples is very similar up to a relative

pressure of 0.030. 2D-NLDFT calculations showed pore volumes (contribution of pores  $< 1$  nm) of 0.165, 0.185 and 0.244 cm<sup>3</sup> g<sup>-1</sup> present in samples CSDHC, CSDHC 280/15 and CSDHC 300/30, respectively. The samples’ pore size distributions were similar, with most pores having a diameter of about 0.6 nm, as predicted by the HS-2D NLDFT model provided in the Micromeritics software (Figure S2). This indicates that hard carbons, CSDHC and CSDHC 280/15, are inferred to be non-porous based on N<sub>2</sub> adsorption; however, they possess ultra-micropores comparable to the activated sample CSDHC 300/30. All three samples contain a similar pore volume accessible to carbon dioxide, but in CSDHC and CSDHC 280/15, these pores are inaccessible (closed) to the nitrogen. Fast diffusions kinetics allow CO<sub>2</sub> to fill the ultra-micropores in CSDHC and CSDHC 280/15. The higher saturation pressure (3.5 MPa) of carbon

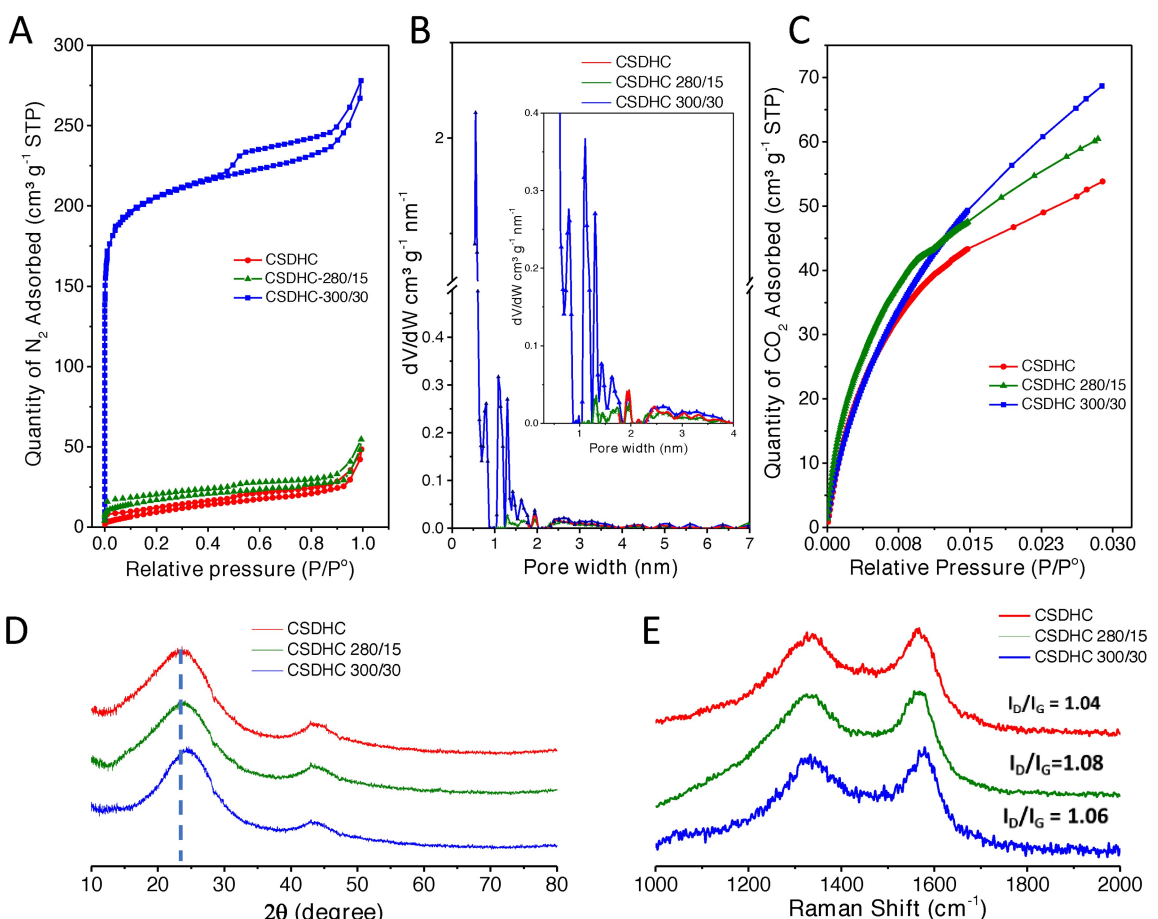


**Figure 2.** A) Nitrogen adsorption/desorption isotherms of CSDHC, CSDHC 280/15 and CSDHC 300/30. CSDHC 300/30 shows a high amount of nitrogen adsorption, indicating its increased surface area. B) pore size distribution of the carbons, CSDHC 300/30 has developed micropores after activation in air. C) carbon dioxide adsorption isotherms taken at 273 K show that all three samples have adsorbed a similar amount of CO<sub>2</sub>. D) XRD patterns of carbon samples with (002) plane marked in dotted line. E) Raman spectra of CSDHC, CSDHC 280/15, and CSDHC 300/30 show very similar  $I_D/I_G$  ratios indicating the chemical nature of the samples is similar.

dioxide limits the possibility of measuring pores higher than 1 nm at 1 atm.<sup>[32,33]</sup>

From the TGA and gas adsorption analysis, we assume that the oxidation at higher temperatures removes the carbon at the pore-mouth and widens the pores, converting the “closed” pores to “open” during air activation. Open pores (accessible to nitrogen) in CSDHC 300/30 are attributed as microporous based on a sharp intake of N<sub>2</sub> at very low partial pressures ( $P/P^0 < 0.1$ ). Opening of the closed pores is evident from micropore volume estimated using N<sub>2</sub> and CO<sub>2</sub>. Micropore volume ( $V_{\text{micro}}$ , pores < 1 nm) of CSDHC 300/30 calculated from nitrogen adsorption gives a value of 0.20 cm<sup>3</sup> g<sup>-1</sup>, which is close to the CO<sub>2</sub> adsorption pore volume of CSDHC (0.165 cm<sup>3</sup> g<sup>-1</sup>) and CSDHC 280/15 (0.185 cm<sup>3</sup> g<sup>-1</sup>). Tarascon’s group used a similar approach on carbon nanofibers to arrive at a converse observation wherein increased pyrolysis temperature closed the micropores and decreased CO<sub>2</sub> intake of carbons but did not change its BET surface area and N<sub>2</sub> adsorption isotherms.<sup>[17]</sup>

The samples were also characterized by powder XRD (PXRD) (Figure 2D). The patterns reveal two distinct reflections in all the cases: one around  $2\theta = 23^\circ$  (002 planes) and the other around  $2\theta = 43^\circ$  (100 planes), as is typically observed for

(partially) disordered carbon matrices. A slight shift towards a higher  $2\theta$  value in the (002) reflection was detected on activating the system for varying periods, commonly correlated with decreasing interlayer distances.<sup>[18,34,35]</sup> But, the thermal annealing at 300 °C is quite low for the rearrangement of curly carbon lattices. Distortion of XRD patterns of turbostratic carbons is influenced by rotation, curvature and translation of the atomic layers. However, a decrease in the peak position of the 002 plane and its broadening (FWHM) is generally considered a result of decreased crystallite size.<sup>[36]</sup> We observed  $2\theta$ : 23.92° (CSDHC), 24.37° (CSDHC 280/15) and 24.68° (CSDHC 300/30) with calculated average  $d$ -spacing of 3.72 (non-activated), 3.64, 3.60 Å using Bragg’s equation,  $2dsin\theta = n\lambda$ , where  $d$  is the average interlayer spacing,  $\theta$  is the diffraction angle,  $n$  is the order of reflection and  $\lambda$  is the wavelength of the incident X-ray excitation beam. The slight shift in XRD of oxidized samples might have been caused by reduced scattering upon removing oxidizable amorphous, less ordered carbon domains. As a control, CSDHC was annealed at 300 °C for 1 h under Ar flow, and no shift in the 002 peak was observed in the XRD pattern. This further indicates that 300 °C is insufficient to rearrange the graphitic planes (Figure S3). R

factor could be an interesting parameter to corroborate our hypothesis. *R* factor is correlated to ratio of single layers to stacked layers, obtained as the ratio of peak intensity of 002 to the baseline (Figure S4). Table S2 shows that the *R* factor increased upon air-activation of the samples, indicating that single layers might preferentially burn off during this step.

Figure 2(E) shows the Raman spectra of samples within the range 1000–2200 cm<sup>-1</sup>. As is expected for hard carbons, both the G-bands (centered at ~1580 cm<sup>-1</sup>) and the D-bands (centered at ~1350 cm<sup>-1</sup>) which could be attributed to vibrations of sp<sup>2</sup>-carbons (ordered) and sp<sup>3</sup>-carbons (disordered), respectively,<sup>[37]</sup> were prominent in all of them. The relative intensities or  $I_D/I_G$  ratios are widely considered as a legit depiction of the extent of disorder and degree of defect concentration in the sample.<sup>[29,38–40]</sup> An analysis of  $I_D/I_G$  (peak intensity) ratios, by fitting the data using the Lorentzian function (Figure S5), (Table 1) conveyed that the activated and non-activated HCs have little variation in disorder upon air-activation. That said, there was no noticeable shift in D-bands and G-bands observed. Raman data further proves that the burn-off has not affected the sample's chemical nature.

Air activation could introduce oxygen functional groups on the carbon. Table 1 summarizes the percentage of C and O in the materials obtained through XPS analysis. Comparable oxygen content in the samples indicates that air oxidation did not introduce additional oxygen functional groups in the material. From the physical characterizations, we could conclude that CSDHC, CSDHC-280/15 and CSDHC-300/30 have similar crystalline and chemical structures but different micro-porosity features.

## Structure of closed pores

As depicted in Scheme 1, the carbon matrix is visualized based on the physicochemical characterization of synthesized carbons. Voids inaccessible to the nitrogen molecules are represented as light yellow regions.

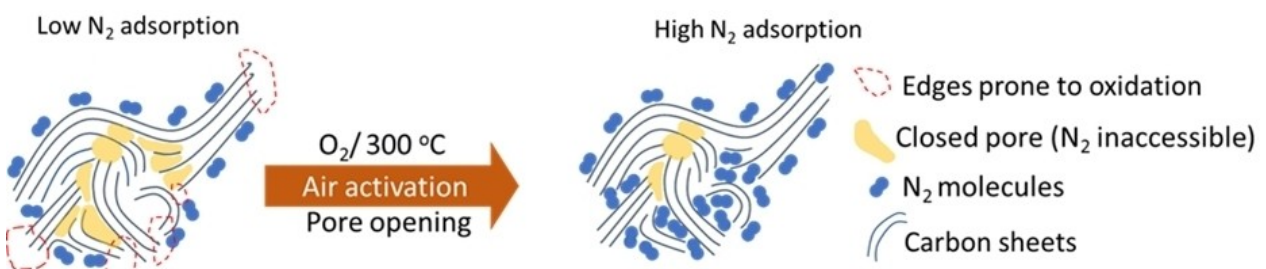
During air oxidation, the regions that are more prone to oxidation, single layers and edges (red dashed curve), react with oxygen and get removed from the matrix. This process widens the pore mouth of the voids and becomes accessible to the nitrogen molecules. A step type increase in the surface area is hence observed for the air-activated samples.

## Electrochemical characterization

The electrochemical performance of non-activated and activated HCs was investigated in half-cell configurations vs. sodium metal. Figure 3(A–C) shows the GCPL profiles (3<sup>rd</sup> cycle) for the non-activated (CSDHC) matrix and those air-activated at 300 °C (CSDHC 300/15) and 280 °C (CSDHC 280/15), respectively, cycled at 100 mA g<sup>-1</sup>. Symmetric charge-discharge curves were observed, evincing decent reversibility of the systems. It was noted that the slope (>0.2 V, marked in green) and plateau (<0.2 V, marked in orange) regions could be discerned distinctly in the voltage profiles prior to air-activation, with a dominant contribution from the slope towards the total reversible capacity.

The behavior of CSDHC-280/15 was noticed to be closely identical to that of the non-activated counterpart, with a slightly reduced plateau region. Interestingly, activating the CSDHC at 300 °C led to an abrupt disappearance of the flat Plateau. There was a notable reduction in the stable discharge capacity from 267 mA h g<sup>-1</sup> to 183 mA h g<sup>-1</sup> even on activating the HC at 300 °C for as short as 3 minutes (Figure S6), throwing hints at a partial/complete deletion of some storage mode which was otherwise possible in the non-activated CSDHC. Differential capacity (dQ/dV) plots (Figure 3D) clearly differentiate the discharge curves into three regions, namely Slope-I (a–b), Plateau (b–c) and Slope-II (c–0.001 V). dQ/dV could supplement the charge/discharge records by showing a peak around 0.07–0.09 V corresponding to the Plateau, which was perceived to diminish in intensity with activation. We could spot a third, subtle region closer to 0 V, marked as "c" in Figure 3(D), according to the second slope in the GCPL profiles.

Table 1. Average <i>d</i> spacing, $I_D/I_G$ ratios and chemical composition of the carbon sample.					
Sample	XRD Average <i>d</i> spacing (002) [Å]	Raman $I_D/I_G$	XPS C [%]	O [%]	C/O
CSDHC	3.72	1.04	92	8	11.5
CSDHC-280/15	3.64	1.08	93	6	15.5
CSDHC-300/30	3.60	1.06	91	8	11.4



Scheme 1. Representation of pore opening in hard carbon during air activation.

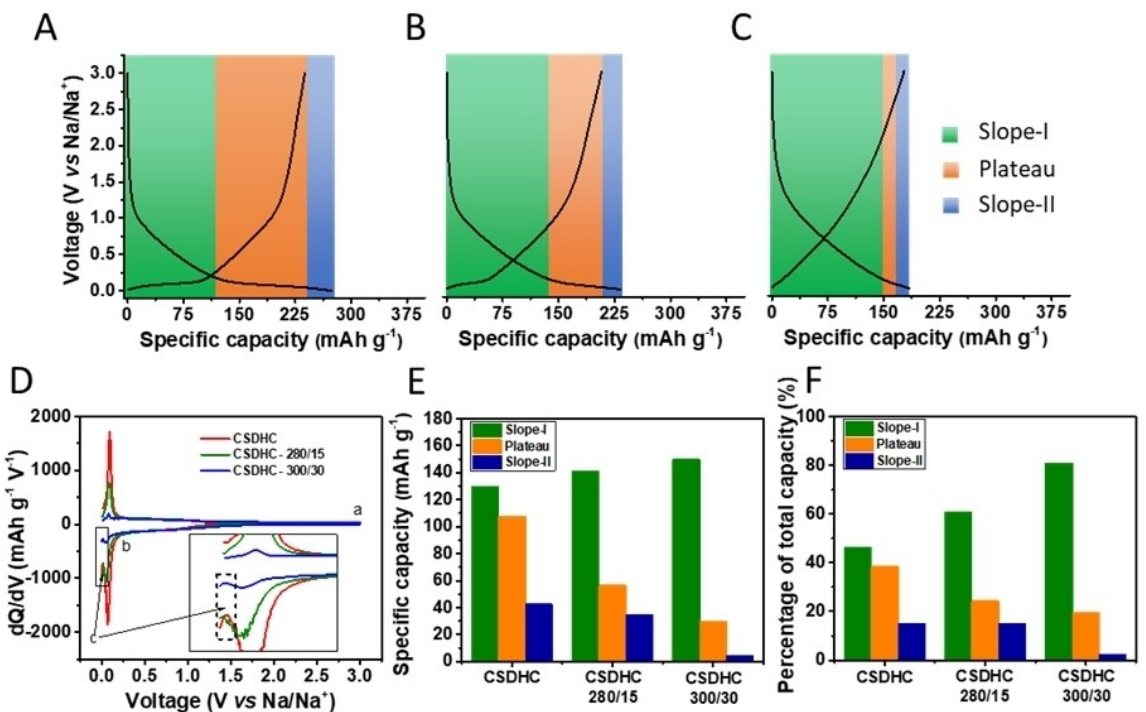


**Figure 3.** Third galvanostatic discharge/charge profiles of A) CSDHC, B) CSDHC 280/15, C) CSDHC 300/30 cycled at 100 mAh g<sup>-1</sup>. Green, orange and blue regions of discharge curves are assigned as the Slope-I, Plateau and Slope -II. D) Differential capacity ( $dQ/dV$ ) of CSDHC, CSDHC 280/15 and CSDHC 300/30 derived from their third discharge/charge profiles. a, b and c are marked to distinguish the change in  $dQ/dV$  value in the graph. E) Specific capacity and F) the percentage of total capacity associated with the Slope-I, Plateau and Slope -II regions in carbon samples.

Figure 3(E), the graph represents specific capacity associated with each region, Slope-I, Plateau and Slope-II, indicates Slope-I region gives more capacity in all the three samples. Even though the Slope-I capacity of CSDHC (130 mAh g<sup>-1</sup>) and CSDHC 300/30 (150 mAh g<sup>-1</sup>) are comparable, their Plateau and Slope-II capacities differ significantly.

While moving from CSDHC to CSDHC-300/30, 46% of the total capacity originating from Slope-I has increased to 81% (Figure 3F); at the same time, Plateau-I capacity dropped from

38% to 16%. Capacity contribution of Slope-II had a share of 15% in CSDHC and dropped to just 2% in CSDHC-300/30.

The Plateau-1 and Slope-II contribution towards the total capacity exhibited a sharp decline with increasing micro-porosity, decreasing to almost negligible contribution for CSDHC 300/30. A comparison of the surface area, initial Coulombic efficiency, (specific) discharge capacities, pore volume and capacity contribution of three different regions are listed (Tables 2 and 3). Poor initial Coulombic efficiency of CSHDC-300/30 is correlated with its high BET surface area. As is

**Table 2.** Porosity features of synthesized carbons.

Sample	Surface area [m <sup>2</sup> g <sup>-1</sup> ] <sup>[a]</sup>	Total pore volume [cm <sup>3</sup> g <sup>-1</sup> ] <sup>[a]</sup>	$V_{\text{micro}} < 1 \text{ nm}$ [cm <sup>3</sup> g <sup>-1</sup> ] <sup>[a]</sup>	$V_{\text{micro}}$ 1–2 nm [cm <sup>3</sup> g <sup>-1</sup> ] <sup>[a]</sup>	$V_{\text{meso}}$ 2–50 nm [cm <sup>3</sup> g <sup>-1</sup> ] <sup>[a]</sup>	$V_{\text{micro}}$ < 1 nm [cm <sup>3</sup> g <sup>-1</sup> ] <sup>[b]</sup>
CSDHC	40	0.068	0	0.003	0.0512	0.165
CSDHC-280/15	60	0.077	0	0.008	0.048	0.185
CSDHC-300/30	655	0.424	0.20	0.092	0.077	0.244

[a] Values calculated from N<sub>2</sub> adsorption isotherm at 77 K. [b] Values calculated from CO<sub>2</sub> adsorption isotherm at 273 K.

**Table 3.** Summary of electrochemical properties of investigated carbon samples.

Sample	First discharge capacity [mAh g <sup>-1</sup> ]	Initial Coulombic efficiency [%]	Slope capacity I [mAh g <sup>-1</sup> ]	Plateau capacity I [mAh g <sup>-1</sup> ]	Slope capacity II [mAh g <sup>-1</sup> ]
CSDHC	415	64	130	108	42
CSDHC-280/15	418	54	141	56	34
CSDHC-300/30	499	37	150	30	4

deductible from the X-ray diffraction analysis, the decreased interlayer distances on activation at 300 °C could have abated the ability of the sodium ions to get inserted. But it is questionable to conclude that this small change in the *d* spacing is not responsible for the disappearance of the plateau region. To rule out the possibility of the disappearance of the Plateau by decreased *d* spacing, we cycled the carbon in an ether-based electrolyte, 1 M NaOTf: DEGDME, which is known for making ternary graphite intercalation compounds through solvent co-intercalation.<sup>[41]</sup> If we assume that the CSDHC-300/30 has improved graphitization as indicated by decreased *d* spacing, then it should give better capacity in NaOTf: DEGDME. There is a clear difference in discharge behavior between CSDHC and CSDHC-300/30, even after using NaOTf: DEGDME. The discharge curves of CSDHC and CSDHC-300/30 were similar to those of the EC: DEC electrolyte (Figure S7). The absence of a plateau region in CSDHC-300/30 even in the diglyme electrolyte confirms that the low potential Plateau is not associated with sodium ion intercalation into graphitic layers. A very similar experiment has been carried out by Bai *et al.* to rule out the possibility of Na intercalation into graphene layers.<sup>[42]</sup>

Further, it is well known that the *R* factor of carbon is considered as a measure of single sheets of carbon to stacked sheets. A higher value of the *R* factor indicates a less number of single sheets. It is known that less graphitic carbon is more prone to oxidation; higher *R* values (Table S2) of our air-activated samples agree with this observation. Upon air activation, less ordered or single-layer sheets of carbon oxidizes and create ultra-micropores without affecting the crystallinity of the bulk material.

Figure S8, a plot of Slope-I, Plateau, and Slope-II capacities as a function of  $I_D/I_G$  demonstrates no noticeable linear relationship between the two observations. It is of no surprise since  $I_D/I_G$  values obtained for the materials were not very different.

In the same way, as in GCPL studies, intermediate cycles (3<sup>rd</sup>) were considered for the comparative analysis of cyclic voltammograms of CSDHC, CSDHC 280/15, and CSDHC 300/30 at 0.1 mVs<sup>-1</sup> (Figure 4A). They displayed a distinct pair of anodic (around 0.1 V) and cathodic (around 0.03 V) peaks, similar to other hard carbon anodes reported. The indicated large areas under the graph for activated samples and hence

an enhancement in the pseudocapacitive behavior, apparently substantiate their completely slopy galvanostatic curves. The peak intensity has also decreased upon activation, agreeing with the diminished plateau region in GCPL curves. We hypothesize that, after opening the closed pores, the electrolyte can access a new surface area, i.e., the internal walls of the pore. Hence, the new surface area should enhance all surface-related phenomena like irreversible capacity loss and capacitive type storage behavior. The inset of Figure 4(A) shows increased capacitive-like storage in the 3–1.5 V region for CSDHC 300/30, where we presume intercalation, as well as capacitive storage, take place. During the activation of CSDHC, the closed micro-pores get converted to open ones, resulting in a loss of considerable capacity contribution in potentials <0.2 V for CSDHC 300/30. The open pores lead to increased capacitive-like storage linked with the surface storage mechanism. Micro-pores in the carbon can store Na ions by adsorbing them to the pore walls upon applying potential.<sup>[43]</sup> By calculating the coulombic efficiency of voltage regions, we observe a significant amount of irreversible loss, as low as 50%, ascribed to 1.5–0.12 V. The irreversible reactions linked with some surface phenomena could explain a plateau-like region in the initial discharge curve of CSDHC, which corresponds to humps observed at 1 V and 0.47 V in dQ/dV (Figure S9D). This is evident from the lengthy first discharge profile of high surface area activated carbon, CSDHC 300/30 (Figure S9C), which starts above 0.8 V. Huge irreversible reactions of the first discharge is reflected as a broad peak (around 0.5 V) in the differential capacity plot. After the first discharge, the surface modification/ newly generated chemical environment positively contributes to the charge storage in the subsequent cycles. After the first discharge, the discharge curve of CSDHC 300/30 gets slightly shifted to higher potential, and the same region is marked in dQ/dV around 1 V. An increase in the area of dQ/dV of the second discharge in the voltage region of 1.5–0.8 V is also noticeable.

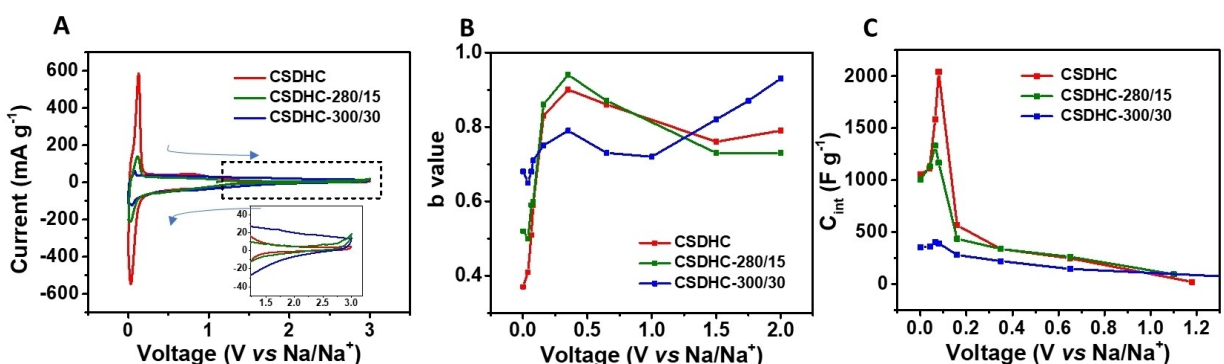


**Figure 4.** A) A comparison of cyclic voltammograms of CSDHC, CSDHC 280/15 and CSDHC 300/30 recorded at a scan rate of 0.1 mVs<sup>-1</sup>. B) *b* value calculated from CVs, using power law  $i = av^b$ , plotted as a function of potential. C) Differential capacities of carbon samples calculated from EIS, plotted as a function of potential.

## Kinetics of Slope-I, Plateau and Slope-II regions

Galvanostatic intermittent titration technique (GITT) or CV analyses are two commonly employed techniques to explore diffusion coefficient and kinetics.<sup>[44]</sup> A necessary condition to employ GITT technique is potential,  $E$ , should linearly depend on  $t^{\frac{1}{2}}$  during the applied current pulse. This condition is not satisfactorily met by the sloping discharge profile of CSDHC 300/30; hence difficult to draw meaningful results. Thus, we prefer to rely on  $b$  value calculations from the CVs of the materials to differentiate diffusion-controlled and surface-controlled reactions.<sup>[45]</sup> In diffusion-limited reactions, current ( $i$ ) values are directly proportional to the square root of scan rate, and for the surface-controlled reaction, it is proportional to scan rate, using the power-law in Equation (1),

$$i = av^b \quad (1)$$

$b$  values obtained from CV analysis is given in Figure 4(B). Electrochemical reactions in all samples become diffusion-controlled ( $b \sim 0.5$ ) around the potential range of 0–0.08 V. The sharp drop in  $b$  values at low potentials for the activated samples (CSDHC 280/15 and CSDHC 300/30) is not as evident as it is for the non-activated carbon (CSDHC). Reaching a minimum value of  $b$  as 0.65 at 0.04 V reflects that the electrochemical environment of CSDHC 300/30 must be hybrid, with both capacitive and faradaic storage. Similar to the “c” region indicated from  $dQ/dV$  graphs of the GCPL curves, an increase in  $b$  value is observed near cut off potentials as well. This suggests that the reaction shifts back to a surface controlled from the diffusion-limited process near zero potentials. The increased  $b$  value indicates the existence of a kinetically faster phenomenon near the zero potential. The lowest  $b$  values (0.65) achieved for CSDHC 300/30 is higher than that for a diffusion-controlled reaction, suggesting a kinetically faster reaction happening in the entire potential region between 3.0–0.001 V. However, it would be safer to perceive that pore (open) filling does not seem to be the mechanism below 0.1 V, as plateau disappears despite the addition of additional porosity.

Electrochemical Impedance Spectroscopy (EIS) can prove imperative as an electro-analytical tool for understanding the kinetics and properties of electrochemical systems if put to the right use, and the technique has been extensively utilized. The differential intercalation capacitance,

$$C_{\text{int}} = \frac{-1}{\omega Z'_{\omega \rightarrow 0}}, \quad (2)$$

can be calculated by extrapolating the imaginary part of the impedance to zero frequency. The plot of differential intercalation capacitance vs. voltage (Figure 4C) peaks at 0.001, 0.04, 0.065 V for CSDHC, CSDHC 280/15 and CSDHC 300/30, respectively. The graph clearly shows the existence of a reaction capable of storing an appreciable amount of Na, happening between 0.001–0.2 V in all the three carbon

materials. Differential capacitance is maximum for CSDHC, followed by CSDHC 280/15 and CSDHC 300/30, and directly correlates with their plateau capacity.

## Understanding charge storage mechanism via solid-state NMR measurements

Solid-state NMR (ssNMR) is a widely used tool to identify the chemical nature of sodium in hard carbon. Electrodes for ssNMR studies were prepared without adding conductive additives to avoid any possible interferences. Half cells of CSDHC were discharged at 20 mA g<sup>-1</sup> current rate to different potentials and held for 2 hours to ensure complete reaction (Figure 5A). A detailed experimental procedure followed for the measurements is given in the experimental section. Figure 5(B) shows ssNMR spectra of CSDHC at potentials, 0.65 V(green), 0.05 V(blue), 0.001 V(red), and -0.16 V(brown), respectively. We observed a signal near 0 ppm for the spectrum collected during the sloping region of the electrochemical process (0.65 V). Signals in this diamagnetic region correspond to the sodium in the electrolyte, pores, and interlayers.<sup>[46]</sup> However, the strong signal of electrolyte (~-10 ppm) makes it difficult to interpret other signals, which appear as shoulders to the major electrolyte signal. As reported in previous studies, sodium inserted in this region is ionic rather than metallic in nature.<sup>[47]</sup> Meanwhile, the spectrum collected in the Plateau region at 0.05 V showed the appearance of a broad signal which spanned over the range of 200–900 ppm. Further lowering of potential (0.001 V) shifted this signal towards higher frequencies with the appearance of another signal near 1133 ppm. Previous reports suggest that this broad signal arises due to the formation of quasi-metallic sodium clusters in the closed pores.<sup>[47,48]</sup> The shift of signals towards higher frequency was contributed by the Knight shift due to the interaction of nuclear spins with the electrons in the Fermi level of the conduction band.

The signal observed at 1133 ppm at 0.001 V indicates the presence of a metallic cluster formed at lower voltages (Slope-II), and was confirmed by comparing the spectra of over-discharged CSDHC at -0.16 V. The comparable resonance frequency (~1133 ppm) of the metallic cluster formed at 0.001 V and that of metallic sodium at -0.16 V suggest analogous Na states in both conditions. A similar observation was reported by Morita *et al.* on Na discharge in sucrose hard carbons.<sup>[49]</sup> Ex-situ <sup>23</sup>Na MAS NMR measurements are performed for the CSDHC 280/15 and CSDHC 300/30 samples with varying depths of discharges, 0.65 V, 0.05 V and 0.001 V (Figure S10). The NMR spectra recorded for the discharged CSDHC 280/15 sample were found to be similar to that of the discharged CSDHC, since both the materials exhibit similar physicochemical properties. Since the closed pores are absent in CSDHC-300/30, no plateau region was observed in the charge/discharge curve, and the NMR spectra recorded for the discharged sample did not show any hump over the range of 200–900 ppm. This indicates the absence of sodium cluster formation in the sample CSDHC-300/30. Hence using ssNMR studies, we were able to show the formation of quasi-metallic

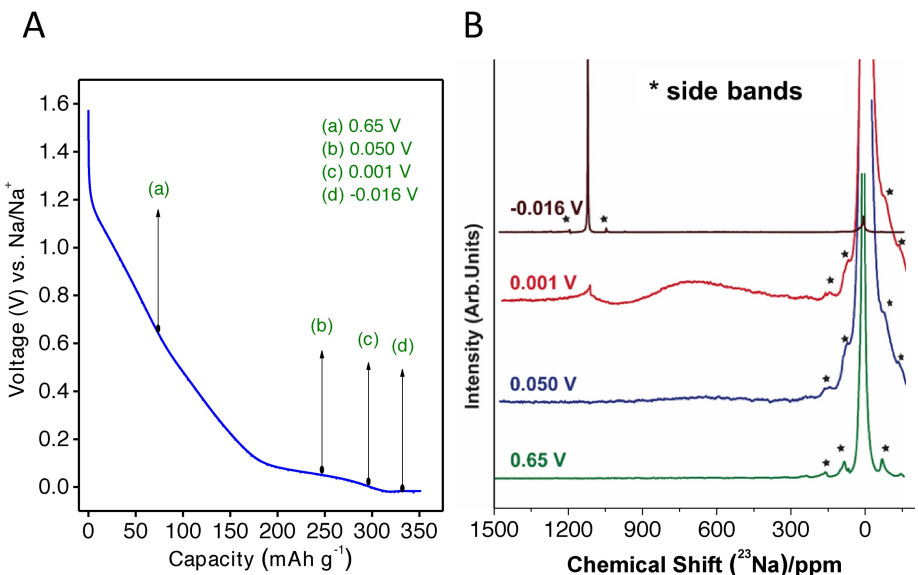


**Figure 5.** A) Discharge curve of CSDHC cell cycled at a current density of 20 mAh g<sup>-1</sup>. Ex-situ <sup>23</sup>Na NMR measurements were carried out for the samples with the depth of discharge at the voltages 0.65, 0.05, 0.001, and -0.016 V. B) <sup>23</sup>Na MAS NMR spectra recorded from samples obtained at different depths of discharge reveal the sodium storage mechanism upon discharge. The slope region (0.65 V) shows only signals in the diamagnetic region. The formation of Knight shifted quasi-metallic and metallic sodium in the closed pores is observed in the plateau region at lower voltages (0.05–0.001 V). The metallic nature of sodium cluster is confirmed from the over discharged spectra taken at -0.016 V. Side bands are highlighted with asterisks.

sodium clusters in the closed pores of carbon samples upon discharge (Plateau), which attains metallic nature at lower voltages (Slope II). These results further support the adsorption/intercalation-pore filling model.

Recent advances in theoretical works associated with the pore-filling mechanism suggest nanopores of diameter 1–2 nm could be ideal for Na cluster formation.<sup>[47,50]</sup> In CSDHC majority of the pores are around 0.5 nm in diameter. Stage II (NaC<sub>16</sub>) mechanism associated with sodium intercalation into expanded domains results in maximum storage of 146 mAh g<sup>-1</sup>. The capacity obtained from the Slope I region for CSDHC, 130 mAh g<sup>-1</sup> (NaC<sub>17</sub>) is close to the ideal value of the stage II intercalation, indicating an intercalation/adsorption-based storage mechanism. Since closed pores generate Plateau and Slope II regions, it will be interesting to relate the number of atoms in the interior of closed pores to the capacity obtained from these regions. The exposed carbon atoms can be calculated by using Equation (2),<sup>[51]</sup>

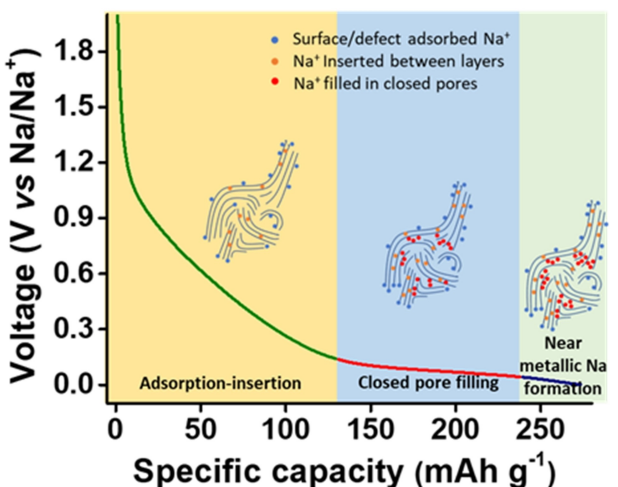
$$\text{Exposed carbon atoms} = \frac{M_w \times S_{\text{BET}}}{2\pi r^2 \times N_A} \quad (3)$$

where,  $M_w$  is the molecular weight of carbon,  $S_{\text{BET}}$  is the BET surface area,  $r$  radius of the carbon atom,  $N_A$  = Avogadro number.

Assuming the cumulative surface area of micropores (< 1.5 nm) in CSDHC 300/30 (660 m<sup>2</sup> g<sup>-1</sup>) equals to the surface area of the closed pores in CSDHC, and substituting it for  $S_{\text{BET}}$  in Equation (2), we find that the interior of the closed pores amounts to 39% of total carbon atoms. Based on this calculation, the obtained capacity of 150.7 mAh g<sup>-1</sup> from the Plateau and Slope II regions corresponds to NaC<sub>5.8</sub>, which is less

than NaC<sub>2</sub>, as calculated by Yong *et al.*<sup>[50]</sup> The deviation from the ideality can be due to the differences in closed pore structure, length of lattices, nucleation centers and overestimation of surface area, etc.

As illustrated in Scheme 2, the sodium storage behavior in hard carbon at different potentials follows three phases. The first slope region, Slope-I, is associated with the adsorption of sodium ions to the defects and surface along with insertion/intercalation into carbon layers. The Plateau region appears when Na<sup>+</sup> fills the “closed” micropores. Na interactions inside the closed pores can be so strong that they form clusters of



**Scheme 2.** Illustration of sodium charge storage mechanism associated with different potential regions.

quasi-metallic and metallic sodium at near-zero voltages resulting in Slope II region.

## Conclusion

In summary, with an aim to elucidate the correlation between micropore volume and sodium storage mechanism in hard carbons, we controllably synthesized carbon materials that retained their bulk crystallinity and chemical nature while differing only in micro-porosity. The electrochemical studies on hard carbon anodes showed a sudden disappearance of the plateau region upon air activation, which is observed due to the opening of nitrogen inaccessible “closed” pores. Our control experiments revealed that the slope region in the discharge curve is associated with sodium ion storage on defects and intercalation into expanded layers, while the plateau portion is associated with the closed pore-filling mechanism. The slope region is fast and capacitive in nature; on the other hand, the plateau region is kinetically sluggish. We presume through our systematic investigation that the closed pores are not electrolyte inaccessible-voids locked in the bulk, but rather “closed pores” whose entrance will be in contact with an electrolyte. At lower potentials, desolvated sodium ions enter through these openings, diffuse and pool inside the pore. Solid-state NMR measurements confirmed that near metallic sodium deposition happens in the closed pores close to 0 V vs. Na. Our findings un-doubtfully confirm the adsorption/intercalation-pore filling model and the significance of closed micropores for generating plateau discharge curves.

## Experimental Section

### Controlled materials synthesis

The bio precursors, coconut sprouts, were freeze-dried and used as per requirements. Samples were initially subjected to pre-carbonization at 400 °C for 2 h under argon atmosphere (200 sccm) in a tube furnace, following which they were observed to be highly alkaline possibly due to presence of alkali metal salts. In fact, it has remained a forsaken fact that hard carbons obtained from biomass hold intrinsic impurities (Na, K salts), necessitating additional treatments.<sup>[31]</sup> They were hence roughly ground into finer particles and washed with DI water until neutral, and subsequently pyrolyzed at 1000 °C for 2 h under argon atmosphere (200 sccm), yielding the hard carbon. The as-pyrolyzed hard carbon has been denoted as CSDHC (coconut sprout derived hard carbon). Activation treatments under mild conditions were carried out at varying temperatures and durations with the ramp rate fixed at 5 °C min<sup>-1</sup> and at a O<sub>2</sub> flow of 80 sccm. Shorthand designations employed for the array of samples prepared can be noted as CSDHC T/M, where T denotes the temperature and M denotes the duration of air-activation in minutes.

### Physical characterization

Raman spectra were recorded using 532 nm laser in Horiba Xplora Plus Raman spectrometer. Samples sprinkled over carbon tape was used for SEM imaging. SEM images are obtained using the Nova

NanoSEM 450, FEI. XRD measurements were performed with a PANalytical XRD equipment using Cu K<sub>α</sub> radiation ( $\lambda = 1.54 \text{ \AA}$ ). For the TEM and HRTEM imaging (FEI Tecnai G2 F30 S-300 kV), a very low concentration of materials dispersed in IPA was dropped across a 400 mesh Cu grid. The X-ray photoelectron spectra (XPS) of the material were obtained using an ESCA Plus spectrometer from Omicron Nanotechnology Ltd, Germany. Prior to the Brunauer-Emmett-Teller (BET) surface area measurements, carbon samples were degassed at 300 °C for 10 h. The Micromeritics 3-Flex surface characterization analyzer is used to detect N<sub>2</sub> adsorption and desorption at 77 K and CO<sub>2</sub> adsorption measurements at 273 K.

### Electrochemical measurements

Electrodes were prepared by coating slurries constituting the active material (~75 wt%), conductive additive/carbon black/Super-P (~15 wt%) and polyvinylidene fluoride/PVDF binder (~10 wt%) in N-methyl pyrrolidone (NMP) on copper foil. The electrodes were dried at 60 °C for 3 h and thereafter 6 h at 120 °C in vacuum. Mass loading of the active material was maintained to be ~1 mg cm<sup>-2</sup>. Half cells were fabricated using standard CR2032 coin cells with sodium metal as the counter electrode, glass-fiber as the separator and 1 M NaClO<sub>4</sub> in 1:1 (volume ratio) ethylene carbonate (EC)-diethyl carbonate (DEC) as the electrolyte. Cells were assembled inside an argon-filled glove box. Electrochemical measurements were performed on a Bio-Logic VMP3 workstation. Galvanostatic cycling with potential limitation (GCPL) and cyclic voltammetric (CV) studies were carried out in a voltage window of 0.001 V vs. Na/Na<sup>+</sup> to 3 V vs. Na/Na<sup>+</sup>. Galvanostatic charge/discharge data were recorded at a current density of 100 mA g<sup>-1</sup> with the cell discharged up to 0.001 V followed by charging up to 3 V. Electrochemical impedance spectroscopic (EIS) data were collected between frequencies ranging from 100 kHz to 10 mHz by applying a sinusoidal perturbation signal of 10 mV amplitude. Impedance spectra were recorded at various potentials while discharging after completing six cycles of charge/discharge to ensure electrochemical equilibrium. The data were analyzed using EC-Lab software in all cases.

### Electrodes for NMR measurements

Active materials were made into a slurry by mixing with PVDF in a 95:5 ratio in NMP. The slurry is then coated on SS discs and dried in 60 °C for 3 h and at 120 °C for 6 h thereafter in a vacuum. Cells were cycled at 50 mA g<sup>-1</sup> to desired potentials and held 3 h to ensure complete reaction. The cells were then carefully disassembled in an argon atmosphere and the electrodes were allowed to dry. The active material was scraped out from the SS disc and packed into 3.2 mm zirconia rotors. <sup>23</sup>Na solid-state NMR (ssNMR) experiments were performed on a Bruker Avance-Neo NMR spectrometer operating at a <sup>1</sup>H Larmor frequency ( $\nu_0$ ) of 500 MHz (<sup>23</sup>Na ( $\nu_0$ ) = 132.34 MHz), equipped with 3.2 mm double resonance (HX) Bruker MAS probe. To avoid oxidation, samples were carefully filled in zirconia rotors inside the glove box. All spectra were recorded at room temperature with the magic angle spinning frequency (MAS) set at 10 kHz. <sup>23</sup>Na chemical shifts were calibrated using 1 M NaCl<sub>aq</sub> at 0 ppm. A one-pulse experiment was measured with a 90° pulse length of 5  $\mu$ s. 2048 transients were collected with a 5 s recycle delay, corresponding to a total experimental time of ~3 h.

## Acknowledgements

**Acknowledgements** Authors are grateful to IISER Thiruvananthapuram for the partial financial support. Support of DST-FIST Govt. of India is acknowledged for the funding of 500 MHz NMR solid-state NMR facility in IISER Thiruvananthapuram.

## Conflict of Interest

The authors declare no conflict of interest.

## Data Availability Statement

The data that support the findings of this study are available from the corresponding author upon reasonable request.

**Keywords:** carbon · closed pores · hard carbons · sodium · sodium-storage mechanism · solids state NMR

- [1] B. Xiao, T. Rojo, X. Li, *ChemSusChem* **2019**, *12*, 133.
- [2] X. Dou, I. Hasa, D. Saurel, C. Vaalma, L. Wu, D. Buchholz, D. Bresser, S. Komaba, S. Passerini, *Mater. Today* **2019**, *23*, 87.
- [3] V. Surendran, R. S. Arya, T. V. Vineesh, B. Babu, M. M. Shaijumon, *J. Energy Storage* **2021**, *35*, 102340.
- [4] V. Surendran, A. Lal, M. M. Shaijumon, *ACS Appl. Mater. Interfaces* **2021**, *13*, 52610.
- [5] Z. E. Yu, Y. Lyu, Y. Wang, S. Xu, H. Cheng, X. Mu, J. Chu, R. Chen, Y. Liu, B. Guo, *Chem. Commun.* **2020**, *56*, 778.
- [6] D. A. Stevens, J. R. Dahn, *J. Electrochim. Soc.* **2000**, *147*, 4428.
- [7] H. Marsh, R. Menendez, in *Introd. to Carbon Sci.* (Eds.: H. Marsh, I. A. S. Edwards, R. Menendez, B. Rand, S. West, A. J. Hosty, K. Kuo, B. McEnaney, T. Mays, D. J. Johnson, J. W. Patrick, D. E. Clarke, J. C. Crelling, R. J. Gray), Butterworth-Heinemann, **1989**, pp. 37–73.
- [8] H. Yamamoto, S. Muratsubaki, K. Kubota, M. Fukunishi, H. Watanabe, J. Kim, S. Komaba, *J. Mater. Chem. A* **2018**, *6*, 16844.
- [9] P. Bai, Y. He, X. Zou, X. Zhao, P. Xiong, Y. Xu, *Adv. Energy Mater.* **2018**, *8*, 1703217.
- [10] X. Dou, I. Hasa, D. Saurel, C. Vaalma, L. Wu, D. Buchholz, D. Bresser, S. Komaba, S. Passerini, *Mater. Today* **2019**, *23*, 87.
- [11] H. Au, H. Alptekin, A. C. S. Jensen, E. Olsson, C. A. O’Keefe, T. Smith, M. Crespo-Ribadeneyra, T. F. Headen, C. P. Grey, Q. Cai, A. J. Drew, M. M. Titirici, *Energy Environ. Sci.* **2020**, *13*, 3469.
- [12] D. A. Stevens, J. R. Dahn, *J. Electrochim. Soc.* **2000**, *147*, 1271.
- [13] D. A. Stevens, J. R. Dahn, *J. Electrochim. Soc.* **2001**, *148*, A803.
- [14] C. Bommier, T. W. Surta, M. Dolgos, X. Ji, *Nano Lett.* **2015**, *15*, 5888.
- [15] J. M. Stratford, P. K. Allan, O. Pecher, P. A. Chater, C. P. Grey, *Chem. Commun.* **2016**, *52*, 12430.
- [16] J. Ding, H. Wang, Z. Li, A. Kohandehghan, K. Cui, Z. Xu, B. Zahiri, X. Tan, E. M. Lotfabad, B. C. Olsen, D. Mitlin, *ACS Nano* **2013**, *7*, 11004.
- [17] B. Zhang, C. M. Ghimbeu, C. Laberty, C. Vix-Guterl, J. M. Tarascon, *Adv. Energy Mater.* **2016**, *6*, 1501588.
- [18] N. Sun, Z. Guan, Y. Liu, Y. Cao, Q. Zhu, H. Liu, Z. Wang, P. Zhang, B. Xu, *Adv. Energy Mater.* **2019**, *9*, 1901351.
- [19] N. Zhang, Q. Liu, W. Chen, M. Wan, X. Li, L. Wang, L. Xue, W. Zhang, *J. Power Sources* **2018**, *378*, 331.
- [20] Q. Meng, Y. Lu, F. Ding, Q. Zhang, L. Chen, Y. S. Hu, *ACS Energy Lett.* **2019**, *4*, 2608.
- [21] X. Dou, C. Geng, D. Buchholz, S. Passerini, *APL Mater.* **2018**, *6*, 047501.
- [22] H. Moon, M. Zarabeitia, E. Frank, O. Böse, M. Enterría, D. Saurel, I. Hasa, S. Passerini, *Batteries & Supercaps* **2021**, *4*, 960.
- [23] J. Han, I. Johnson, Z. Lu, A. Kudo, M. Chen, *Nano Lett.* **2021**, *21*, 6504.
- [24] D. Cheng, X. Zhou, H. Hu, Z. Li, J. Chen, L. Miao, X. Ye, H. Zhang, *Carbon* **2021**, *182*, 758.
- [25] C. Bommier, T. W. Surta, M. Dolgos, X. Ji, *Nano Lett.* **2015**, *15*, 5888.
- [26] Y. Li, Y. Lu, Q. Meng, A. C. S. Jensen, Q. Zhang, Q. Zhang, Y. Tong, Y. Qi, L. Gu, M. M. Titirici, Y. S. Hu, *Adv. Energy Mater.* **2019**, *9*, 1.
- [27] M. M. R. Sreelekshmi, K. P. Sayooja, A. P. Souparnika, K. Sowparnika, T. S. Pournami, K. R. Sabu, B. R. Rajesh, R. P. Chandran, *MOJ Food Process Technol.* **2018**, *6*, 445.
- [28] J. Ding, H. Wang, Z. Li, K. Cui, D. Karpuzov, X. Tan, A. Kohandehghan, D. Mitlin, *Energy Environ. Sci.* **2015**, *8*, 941.
- [29] F. Xie, Z. Xu, A. C. S. Jensen, H. Au, Y. Lu, V. Araullo-Peters, A. J. Drew, Y. S. Hu, M. M. Titirici, *Adv. Funct. Mater.* **2019**, *29*, 1901072.
- [30] M. Thommes, K. Kaneko, A. V. Neimark, J. P. Olivier, F. Rodriguez-Reinoso, J. Rouquerol, K. S. W. Sing, *Pure Appl. Chem.* **2015**, *87*, 1051.
- [31] J. S. Xue, J. R. Dahn, *J. Electrochim. Soc.* **1995**, *142*, 3668.
- [32] P. I. Ravikovich, A. Vishnyakov, R. Russo, A. V. Neimark, *Langmuir* **2000**, *16*, 2311.
- [33] A. Beda, C. Vaulot, C. M. Ghimbeu, *J. Mater. Chem. A* **2021**, *9*, 937.
- [34] J. Górká, C. Vix-Guterl, C. Matei Ghimbeu, *C* **2016**, *2*, 24.
- [35] Y. Jin, S. Sun, M. Ou, Y. Liu, C. Fan, X. Sun, J. Peng, Y. Li, Y. Qiu, P. Wei, Z. Deng, Y. Xu, J. Han, Y. Huang, *ACS Appl. Energ. Mater.* **2018**, *1*, 2295.
- [36] Z. Q. Li, C. J. Lu, Z. P. Xia, Y. Zhou, Z. Luo, *Carbon* **2007**, *45*, 1686.
- [37] M. Inaba, H. Yoshida, Z. Ogumi, T. Abe, Y. Mizutani, M. Asano, *J. Electrochim. Soc.* **1995**, *142*, 20.
- [38] A. Sadezky, H. Muckenhuber, H. Grothe, R. Niessner, U. Pöschl, *Carbon* **2005**, *43*, 1731.
- [39] A. C. Ferrari, J. Robertson, *Phys. Rev. B* **2000**, *61*, 95.
- [40] H. Lu, F. Ai, Y. Jia, C. Tang, X. Zhang, Y. Huang, H. Yang, Y. Cao, H. Lu, Y. Jia, H. Yang, Y. Cao, F. Ai, C. Tang, X. Zhang, Y. Huang Dong, Guan McNair, *Small* **2018**, *14*, 1802694.
- [41] R. Dong, L. Zheng, Y. Bai, Q. Ni, Y. Li, F. Wu, H. Ren, C. Wu, *Adv. Mater.* **2021**, *33*, 2008810.
- [42] P. Bai, Y. He, X. Zou, X. Zhao, P. Xiong, Y. Xu, *Adv. Energy Mater.* **2018**, *8*, 1703217.
- [43] A. Karatrantos, Q. Cai, *Phys. Chem. Chem. Phys.* **2016**, *18*, 30761.
- [44] B. Babu, M. M. Shaijumon, *Electrochim. Acta* **2020**, *345*, 136208.
- [45] B. Babu, S. G. Ullattil, R. Prasannachandran, J. Kavil, P. Periyat, M. M. Shaijumon, *ACS Sustainable Chem. Eng.* **2018**, *6*, 5401.
- [46] K. Gotoh, *Batteries & Supercaps* **2021**, *4*, 1267.
- [47] J. M. Stratford, A. K. Kleppe, D. S. Keeble, P. A. Chater, S. S. Meysami, C. J. Wright, J. Barker, M. M. Titirici, P. K. Allan, C. P. Grey, *J. Am. Chem. Soc.* **2021**, *143*, 14274.
- [48] J. M. Stratford, P. K. Allan, O. Pecher, P. A. Chater, C. P. Grey, *Chem. Commun.* **2016**, *52*, 12430.
- [49] R. Morita, K. Gotoh, K. Kubota, S. Komaba, K. Hashi, T. Shimizu, H. Ishida, *Carbon* **2019**, *145*, 712.
- [50] Y. Youn, B. Gao, A. Kamiyama, K. Kubota, S. Komaba, Y. Tateyama, *npj Comput. Mater.* **2021**, *7*, 1.
- [51] C. Bommier, W. Luo, W. Y. Gao, A. Greaney, S. Ma, X. Ji, *Carbon* **2014**, *76*, 165.

Manuscript received: July 8, 2022

Accepted manuscript online: August 3, 2022

Version of record online: August 24, 2022